

Spin-dependent optical superlattice

Bing Yang,^{1,2} Han-Ning Dai,^{1,2} Hui Sun,^{1,2} Andreas Reingruber,² Zhen-Sheng Yuan,^{1,2,3,4,*} and Jian-Wei Pan^{1,2,3,4,†}

¹Hefei National Laboratory for Physical Sciences at Microscale and Department of Modern Physics,
University of Science and Technology of China, Hefei, Anhui 230026, China

²Physikalisches Institut, Ruprecht-Karls-Universität Heidelberg, Im Neuenheimer Feld 226, 69120 Heidelberg, Germany

³CAS-Alibaba Quantum Computing Laboratory, Shanghai 201315, China

⁴CAS Centre for Excellence and Synergetic Innovation Centre in Quantum Information and Quantum Physics,
University of Science and Technology of China, Hefei, Anhui 230026, China

(Received 16 March 2017; published 20 July 2017)

We propose and implement a lattice scheme for coherently manipulating atomic spins. Using a vector light shift and a superlattice structure, we demonstrate experimentally its capability on addressing spins in double wells and square plaquettes with subwavelength resolution. The quantum coherence of spin manipulations is verified through measuring atom tunneling and spin exchange dynamics. Our experiment presents a building block for engineering many-body quantum states in optical lattices for realizing quantum simulation and computation tasks.

DOI: 10.1103/PhysRevA.96.011602

Ultracold atoms in optical lattices constitute a promising system for creating multipartite entangled states [1,2], which is an essential resource for quantum information processing [3,4]. As the neutral atoms prepared in the Mott insulating state consist of highly ordered quantum registers [5,6], multipartite entanglement can be generated via parallelly addressing single atoms together with two-body interactions [3,7–9]. Following this route, sublattice addressing and $\sqrt{\text{SWAP}}$ operations in double wells (DWs) were demonstrated [10,11], where atomic spins in decoupled DW arrays were addressed by utilizing the spin-dependent effect [10,12]. However, extending these entangled pairs to a one-dimensional (1D) chain or a two-dimensional (2D) cluster remains challenging due to the lack of control over interwell couplings [13]. In this context, a bichromatic lattice referred to as a “superlattice” provides an alternative degree of freedom to connect the entangled pairs by tuning the relative lattice phase [14,15]. Besides the $\sqrt{\text{SWAP}}$ operation in such superlattices, site-selective single-qubit addressing is further required to create multipartite cluster states for measurement-based quantum computation [4,8].

In this Rapid Communication, we demonstrate a spin-dependent optical superlattice for coherently addressing and manipulating atomic spins. Such a lattice configuration allows one to first address even or odd rows of spins in parallel and then create entangled pairs, as well as to enable a further connection of the pairs to form a multipartite entangled state with high fidelity. This configuration offers an efficient way for spin addressing in higher dimensions [16] and meanwhile becomes a powerful tool in detecting the quantum correlations of entangled states [17].

The optical lattice consists of two far-detuned lasers, one generating a local effective magnetic gradient, and the other one isolating the system into DWs and forming imbalanced structures for different spin states. To illustrate the spin-dependent optical potential, we consider an alkali-metal atom placed inside a far-detuned laser field [12,18,19]. The

monochromatic light field has a complex notation $\mathbf{E}(\mathbf{x}, t) = \vec{E}(\mathbf{x}) \exp(-i\omega t) + \text{c.c.}$, where \vec{E} represents the positive-frequency part with the driving frequency ω . The optical potential for the atom in the ground state reads $V(\mathbf{x}) = -\vec{E}^*(\mathbf{x}) \cdot \boldsymbol{\alpha} \cdot \vec{E}(\mathbf{x})$. Here, $\boldsymbol{\alpha}$ is the polarizability tensor with irreducible scalar α_s and vector components α_v that contribute to the potential herein [12]. For ^{87}Rb with states indexed by the hyperfine F and magnetic m_F quantum numbers, the optical potential is a combination of a scalar and vector light shift, $V = V_s + V_v$. The scalar part $V_s = -\alpha_s |\vec{E}|^2$ is state independent and proportional to the laser intensity. The vector part $V_v = i\alpha_v (\vec{E}^* \times \vec{E}) \cdot \vec{F}$ is state dependent and can be regarded as an effective Zeeman shift with $\vec{B}_{\text{eff}} \propto i(\vec{E}^* \times \vec{E})$. This vector potential depends on the laser polarization and the quantization axis of the angular momentum \vec{F} . It vanishes for linearly polarized light or for $m_F = 0$ magnetic sublevels.

Our one-dimensional superlattice is formed by superimposing two optical standing waves differing in the period by a factor of 2 (see Fig. 1). The lattices are respectively marked as “short lattice” and “long lattice” by their wavelengths λ_s and λ_l . Without any vector light shift, the optical dipole potential can be written as $V(x) = V_s \cos^2(kx) - V_l \cos^2(kx/2 + \varphi)$, with $k = 2\pi/\lambda_s$, the wave number and φ the relative phase between the lattices. The relative phase φ is controlled by tuning the laser frequency of the long lattice. The spin dependence arising from the laser polarization is controlled by an electro-optical modulator (EOM). Figure 1(a) shows the setup of a superlattice that consists of a blue-detuned ($\lambda_s = 767$ nm) and a red-detuned ($\lambda_l = 1534$ nm) lattice, where the polarization of the short lattice is denoted as a “lin- θ -lin” configuration [20,21]. The local polarization can be decomposed into σ^\pm and π components referring to the orientation of the magnetic axis. When the magnetic axis is along x , the optical potential has a spin-dependent short-lattice term and a scalar long-lattice term,

$$V_j(x) = V_{s,j} \left[A_j^+ \cos^2 \left(kx + \frac{\theta}{2} \right) + A_j^- \cos^2 \left(kx - \frac{\theta}{2} \right) \right] - V_l \cos^2 \left(\frac{kx}{2} + \varphi \right). \quad (1)$$

*yuanzs@ustc.edu.cn

†pan@ustc.edu.cn

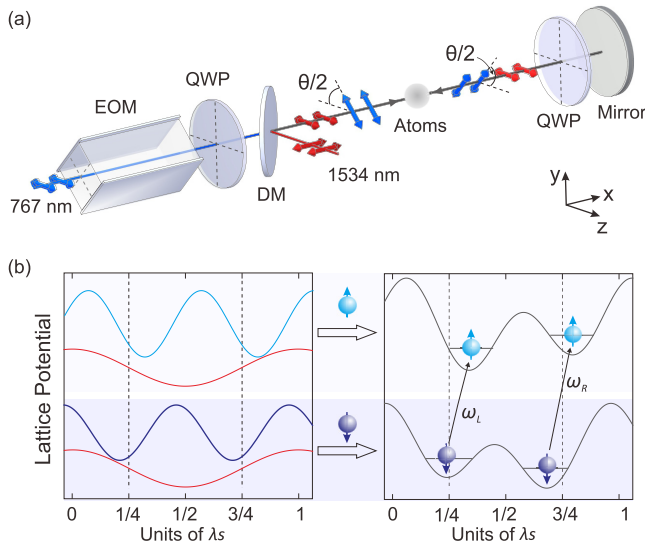


FIG. 1. Schematic of experimental setup and spin-dependent optical potentials. (a) The 1D superlattice is formed by overlapping two lattices on a dichroic mirror (DM). The incident polarization of the short lattice is controlled by an electro-optical modulator (EOM) and a quarter-wave plate (QWP). The polarization of the reflected laser is in mirror symmetry with that of the incident beam with respect to the x - z plane. (b) The DWs are formed by a combination of short- and long-lattice potentials. The polarized short lattice leads to a shift of the potential minimum in opposite directions for $|\uparrow\rangle$ and $|\downarrow\rangle$. The long lattice provides a period doubling potential and breaks the symmetry of the transition frequency in the DWs. Here, the optical lattices in the y and z directions are not shown.

For a certain spin state j , the parameters A^+ and A^- are mainly determined by laser detuning of the short lattice. We can define the spin states of ^{87}Rb as $|\downarrow\rangle \equiv |F=1, m_F=-1\rangle$ and $|\uparrow\rangle \equiv |F=2, m_F=-2\rangle$. The parameters for the $|\downarrow\rangle$ state are $A_{\downarrow}^+ = 0.55$ and $A_{\downarrow}^- = 0.45$, while for spin $|\uparrow\rangle$ they are $A_{\uparrow}^+ = 0.40$ and $A_{\uparrow}^- = 0.60$.

The spin-dependent term of Eq. (1) equals a periodical potential $V_{s,j}[A_{\text{eff}} \cos^2(kx + \theta_{\text{eff}}/2) + (1 - A_{\text{eff}})/2]$, with an effective depth $A_{\text{eff}} = \sqrt{\cos^2 \theta + (A^+ - A^-)^2 \sin^2 \theta}$ and phase shift $\theta_{\text{eff}} = \tan^{-1}[(A^+ - A^-) \tan \theta]$. For $\theta = \pi/2$, the effective depth acquires a minimum $A_{\text{eff}} = |A^+ - A^-|$ and the trap bottom shifts for $\lambda_s/4$. Until now, the coupling frequencies between $|\downarrow\rangle$ and $|\uparrow\rangle$ for each well in the spin-dependent short lattice are the same [see Fig. 1(b), left]. Interestingly, the left-right symmetry breaks as the long lattice adds a local potential to the DW unit and creates two different coupling frequencies ω_L and ω_R as in Fig. 1(b), right. The DWs have imbalanced structures and tilt along opposite directions for spins $|\downarrow\rangle$ and $|\uparrow\rangle$. The superlattice with spin dependence therefore provides another degree of freedom for manipulating the atoms in the left or right wells of the DWs. Meanwhile, it creates a strong effective magnetic gradient field on the order of ~ 250 G/cm, which can be switched on and off with a fast speed (the EOM ramping time is $500 \mu\text{s}$) while it does not induce any unwanted eddy current. The lattice residual potential at small angles $(1 - \cos \theta)$ is proportional to the second order of the bias $\sim \theta^2$, inducing a fairly small increase of the ground-band heating compared with that in the unbiased

potential. Since the EOM locates before the combining of the bichromatic lasers, it does not cause an intensity imbalance of the incident and reflected beams [10,22]. Such a structure does not affect the long lattice, therefore circumventing unwanted phase fluctuations.

We implement such a spin-dependent superlattice to realize the spin addressing. The experiment starts with a Bose-Einstein condensate of ^{87}Rb with around 2×10^5 atoms in the $|F=1, m_F=-1\rangle$ hyperfine state [16,17]. Then, the condensate is adiabatically loaded into a single layer of a pancake-shaped trap, which is generated by interfering two laser beams with a wavelength of λ_s and an intersection angle of 11° . Subsequently, we ramp up the 2D short lattice along x and y . As the lattice depths rise to $25E_r$, atoms are thereby localized into individual sites and enter an insulator state. Here, $E_r = \hbar^2/(2m\lambda_s^2)$ denotes the recoil energy of the blue-detuned laser, with \hbar the Planck constant and m the mass of the atom. The x and y short lattices have a frequency difference of 160 MHz to avoid the interference of these two dimensions. The filling number per lattice site and the strength of the on-site interaction are mainly controlled by adjusting the depth of the 4- μm -period ‘‘pancake’’ lattice.

For one-dimensional spin addressing in the DWs, we prepare atoms in a spin-dependent superlattice and then apply a Rabi flopping pulse on the atoms. After initialization of the insulating state, the short and long lattices along x are ramped up to $60E_r$ and $21E_r$, respectively. The long lattice divides the atoms into balanced DW units with $\varphi = 0^\circ$. The quantization axis is set to x and the phase of EOM is tuned to $\theta = 45^\circ$, forming an energy shift between the left and right wells as in Fig. 1. Subsequently, we apply a 167- μs microwave π pulse to couple the spins $|\downarrow\rangle$ and $|\uparrow\rangle$. After the state addressing, the spin dependence is turned off by returning the EOM to $\theta = 0^\circ$. Two alternative methods, site-resolved band mapping [11,14] and *in situ* imaging, are adapted to detect the spin populations (see the Appendix). Figure 2(a) shows the band mapping patterns of different spin states and site occupations, and the efficiencies for generating spin features $|\uparrow, \downarrow\rangle$ and $|\downarrow, \uparrow\rangle$ are 92(7)% and 91(5)%, respectively. However, we notice that the spin-exchange dynamics during the band mapping could reduce the detection fidelity [11,14]. Since only $|\uparrow\rangle$ reacts with the imaging cycling transitions, we also use *in situ* absorption imaging to detect the quantum states. Figure 2(b) shows the spectroscopy of site-selective addressing, where the transition peaks of the left and right DWs are separated for 18.7(1) kHz.

This spin addressing technique is extended to a two-dimensional system by implementing the superlattices on both directions. The long-lattice light along y is generated by another laser source with ~ 11 GHz detuning from the frequency of the x long-lattice laser. Therefore, the x and y lattices have no crosstalk and their frequencies can be controlled individually. Atoms are initially prepared in the insulating state in the short lattices, then the long lattices are ramped up to form arrays of isolated square plaquettes. We perform 2D spin addressing along each dimension in sequence, showing the capability to create a Néel antiferromagnetic state inside the plaquettes. For this, the quantization axis is first set along y , and the atoms in two sites [marked as C and D in Fig. 3(a)] of a plaquette are flipped by a MW π pulse in the spin-dependent potential. Then we switch the magnetic

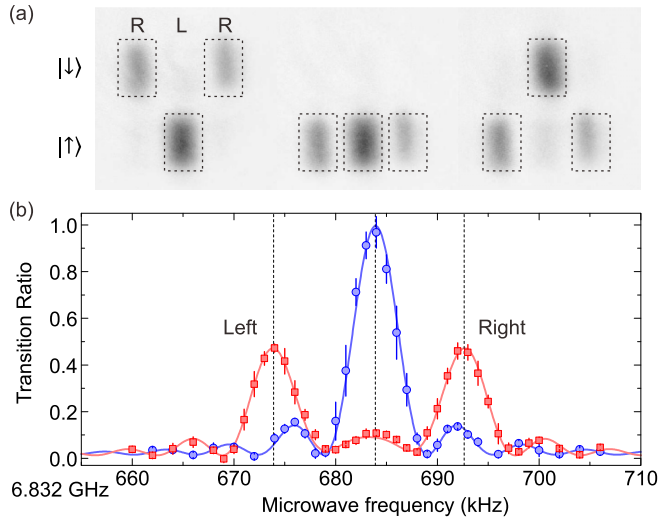


FIG. 2. One-dimensional spin addressing. (a) Band mapping of the spin states in DWs. Atoms in the left and right wells are mapped onto different Bloch bands. We then spatially separate the spin states by a Stern-Gerlach pulse. The left (right) picture is after spin flipping of the atoms in the left (right) sites. In the central picture, all the atoms are flipped by the MW pulse. (b) Spectroscopy of the microwave transitions. The red and blue curves are the transition ratios with and without the spin-dependent effect, respectively. The splitting of the resonance frequency between the DW sites is 18.7(1) kHz.

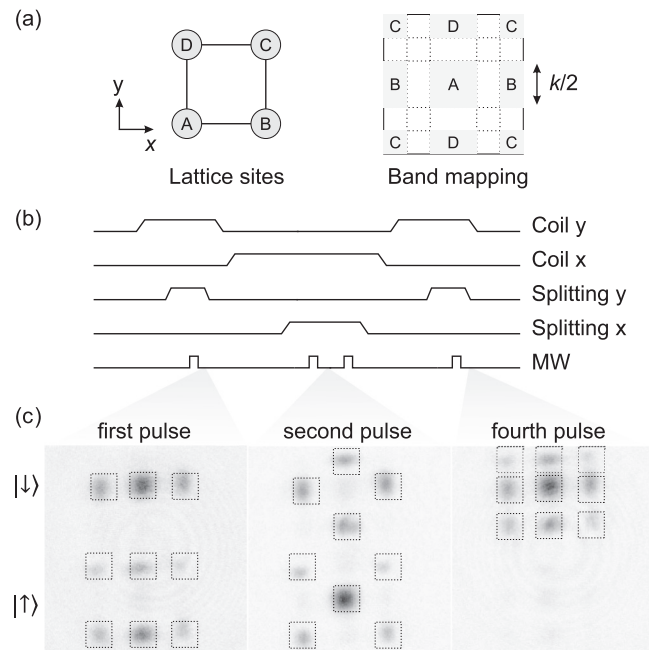


FIG. 3. Two-dimensional spin addressing. (a) Lattice sites are marked as A–D in each square plaquette. The band mapping pattern shows the distribution of each site in momentum space. (b) The experimental sequence of 2D spin flipping. Before each MW pulse, the quantization axis is set and energy splitting is established. The first pulse flips sites C and D, the second pulse flips sites A and D, and the third and fourth pulses recover the initial state. (c) Band mapping pattern after 2D spin addressing. $|\uparrow\rangle$ and $|\downarrow\rangle$ states are spatially separated by a Stern-Gerlach pulse. The pattern after the second MW pulse shows both diagonal sites A and C transit to $|\uparrow\rangle$.

axis to x and tune the energy splitting to the desired value. A second MW π pulse flips the spin states of sites A and D. After these two operations, atoms in the diagonal sites A and C are transferred to $|\uparrow\rangle$, achieving a $|\uparrow, \downarrow, \uparrow, \downarrow\rangle$ spin configuration with site notations from A to D. For further calibrations, we then apply a third and a fourth pulse to recover the initial state by addressing x and y in the same fashion. Figure 3 shows the addressing sequences and the corresponding signals, where 2D band mapping and a Stern-Gerlach gradient analogous to the 1D case are applied to resolve the plaquette spins. The same 2D spin addressing can also be realized with a single MW pulse by setting the same transition frequencies for sites A and C [16]. From the *in situ* imaging, we calibrate the addressing efficiency of the spin state $|\uparrow, \downarrow, \uparrow, \downarrow\rangle$ to be 92(2)%.

To demonstrate coherent control of the spin dynamics, we study the single-atom tunneling and spin-exchange process in DW systems. Atom tunneling J represents the nearest-neighbor hopping term in the Bose-Hubbard model [2]. The spin-exchange dynamics is driven by a second-order interaction described by the Heisenberg spin model $\hat{H} = -2J_{\text{ex}}\hat{S}_L \cdot \hat{S}_R$ [7, 14, 17]. By isolating the atoms into DW units, we reduce the Hilbert space close to two-level systems and thereby observe the evolutions.

The starting point of the experiment is a Mott insulator state with near unity filling. To observe single-atom tunneling, the atoms in the left sites are flipped and removed from the lattices, resulting in single fillings in the right sites and zero fillings in the left sites. We then lower the barrier of DWs and let the system evolve. After a time t the spin states are frozen by ramping up the DW barriers and we address the left sites again. The signal of the following absorption imaging has only contributions from atoms which have tunneled to the left sites, $P_L(t) = \langle \hat{n}_{\downarrow, L} \rangle$ (here, $\hat{n}_{\downarrow, L}$ represents the number operator of the left site). For short- and long-lattice depths of $11.9(1)E_r$ and $10.1(1)E_r$ during the evolution, the theoretical tunneling strength $J/h = 377(8)$ Hz matches the experimental results, as can be seen in Fig. 4(a). The atoms are well isolated in DWs and can oscillate for six cycles without any discernible decay, indicating the excellent coherence of the system. Since the frequency is sensitive to the difference of the left- and right-well energy levels, atom tunneling constitutes a sensitive tool to calibrate the superlattice phase φ .

In the limit of $J \ll U$ (U is the on-site interaction of the Bose-Hubbard model), the spin-exchange interaction can be well described by a two-level system with an interaction strength $J_{\text{ex}} = 2J^2/U$ [7, 14]. To maximize the spin-exchange amplitude, spin-dependent splitting should be minimized to keep the states $|\uparrow, \downarrow\rangle$ and $|\downarrow, \uparrow\rangle$ degenerate. Thus, besides setting the EOM to $\theta = 0^\circ$, we also set the quantization axis to z during the spin-exchange evolutions. The lattice parameters for spin exchange are $V_s = 17.0(1)E_r$ and $V_l = 10.0(1)E_r$, resulting in a superexchange interaction strength of $J_{\text{ex}}/h = 17.8(8)$ Hz. We monitor the dynamics using the Néel order parameter $N_z = (n_{\uparrow L} + n_{\downarrow R} - n_{\uparrow R} - n_{\downarrow L})/2$, where $n_{\uparrow, \downarrow; L, R} = \langle \hat{n}_{\uparrow, \downarrow; L, R} \rangle$ denotes the corresponding quantum mechanical expectation values. Figure 4(b) shows such a spin-exchange oscillation with a high contrast. On the other hand, the spin-dependent effect can be used to suppress the spin-exchange process by breaking the degeneracy of the spin states $|\uparrow, \downarrow\rangle$ and $|\downarrow, \uparrow\rangle$. When the quantization axis is set

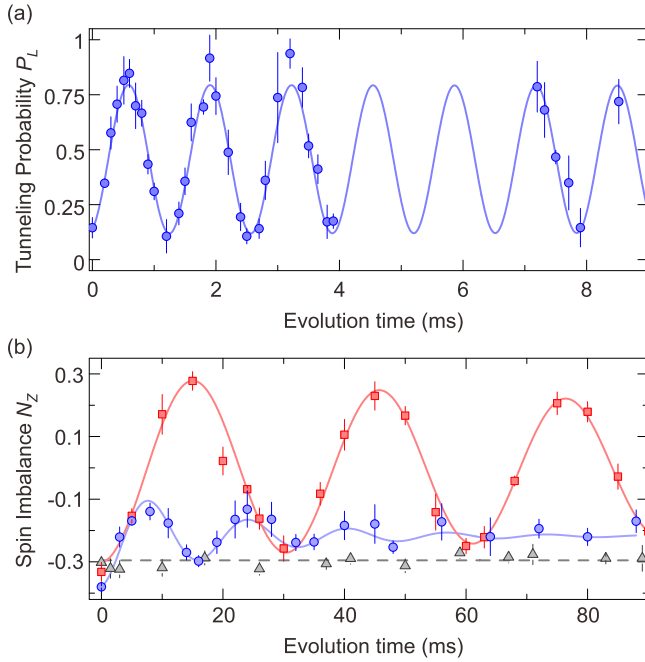


FIG. 4. Dynamics of (a) single-atom tunneling and (b) superexchange. (a) The quantum states in DWs are initialized to $|0, \downarrow\rangle$ by removing the atoms in the left sites. We measure the tunneling dynamics by monitoring the occupancy probability of atoms in the left sites. The oscillation lasts for six cycles with a period of 1.32 ms. (b) Free evolution and suppressions of superexchange dynamics. The red curve is under the Hubbard parameters of tunneling $J/h = 103(2)$ Hz, on-site interaction $U/h = 1191(2)$ Hz, while the blue and the gray curves correspond to the dynamics with extra energy shifts of $\delta/h = 60$ Hz and $\delta/h = 300$ Hz, respectively. The error bars represent a $\pm 1\sigma$ standard deviation.

to the lattice direction, controlling the EOM can induce an energy shift δ between these two spin states. As shown in Fig. 4(b), the oscillations between states $|\uparrow, \downarrow\rangle$ and $|\downarrow, \uparrow\rangle$ are dramatically suppressed as $\delta > J_{\text{ex}}$. Such phenomena can be explained by a detuned Rabi oscillation in a two-level system, where the frequency becomes larger $\sqrt{4J_{\text{ex}}^2 + \delta^2}$ and the amplitude becomes smaller $4J_{\text{ex}}^2 / (4J_{\text{ex}}^2 + \delta^2)$. The suppression of lower-order dynamics can be used to explore some high-order spin interactions, such as four-body ring-exchange

interactions [16]. Another important feature is the flexibility to tune the phase of entangled Bell states via controlling this energy bias δ [17].

In summary, we have developed a spin-dependent optical superlattice for tailoring the atomic states and spin interactions. Such a lattice provides a platform for engineering quantum states in two dimensions and detecting spin correlations with *in situ* imaging, e.g., generating Bell states and observing four-body ring-exchange interactions [16,17]. With the capability of spin addressing and manipulation, one can explore various quantum many-body models, such as spin interactions [14,23], artificial gauge fields [24–27], and out-of-equilibrium dynamics [28] with a different approach in quantum state initializations and detections. Moreover, our spin-dependent lattice could also be used in atom cooling [29,30], which offers intriguing prospects for future research on spin models and quantum magnetism [31–33].

This work has been supported by the MOST (2016YFA0301600), the NNSFC (91221204, 91421305), and the Chinese Academy of Sciences.

APPENDIX : SITE-RESOLVED BAND MAPPING IN A SUPERLATTICE

To detect the atom and spin population on different lattice sites, we utilize a site-resolved band mapping sequence [11,14] in the optical superlattice. After the state preparation, the barriers between the intra-DWs are ramped up to freeze the quantum states. We then map the atoms in the left and right DWs onto different Bloch bands and measure the occupation via absorption imaging after a time of flight. The superlattice phase φ is first tuned adiabatically to 70° , matching the energy of the right ground band with the highly excited band of the left site. Then the DWs are merged by lowering the short-lattice barrier during $300 \mu\text{s}$, whereafter the x long lattice and y short lattice are ramped down during $600 \mu\text{s}$. Finally, we apply a magnetic gradient during the time of flight to separate the spins (Stern-Gerlach separation), mapping out the spin and site populations into different Brillouin zones. Figure 2(a) shows the band mapping patterns of different spin states and site occupations. The size of the Brillouin zones along x is half of the size along the y direction, reflecting the double-lattice constant of the long lattice.

- [1] I. Bloch, *Nature (London)* **453**, 1016 (2008).
- [2] D. Jaksch, H. J. Briegel, J. I. Cirac, C. W. Gardiner, and P. Zoller, *Phys. Rev. Lett.* **82**, 1975 (1999).
- [3] M. A. Nielsen and I. L. Chuang, *Quantum Computation and Quantum Information* (Cambridge University Press, Cambridge, U.K., 2010).
- [4] R. Raussendorf and H. J. Briegel, *Phys. Rev. Lett.* **86**, 5188 (2001).
- [5] W. S. Bakr, A. Peng, M. E. Tai, R. Ma, J. Simon, J. I. Gillen, S. Fölling, L. Pollet, and M. Greiner, *Science* **329**, 547 (2010).
- [6] J. F. Sherson, C. Weitenberg, M. Endres, M. Cheneau, I. Bloch, and S. Kuhr, *Nature (London)* **467**, 68 (2010).
- [7] L. M. Duan, E. Demler, and M. D. Lukin, *Phys. Rev. Lett.* **91**, 090402 (2003).
- [8] B. Vaucher, A. Nunnenkamp, and D. Jaksch, *New J. Phys.* **10**, 023005 (2008).
- [9] K. Inaba, Y. Tokunaga, K. Tamaki, K. Igeta, and M. Yamashita, *Phys. Rev. Lett.* **112**, 110501 (2014).
- [10] P. J. Lee, M. Anderlini, B. L. Brown, J. Sebby-Strabley, W. D. Phillips, and J. V. Porto, *Phys. Rev. Lett.* **99**, 020402 (2007).
- [11] M. Anderlini, P. J. Lee, B. L. Brown, J. Sebby-Strabley, W. D. Phillips, and J. V. Porto, *Nature (London)* **448**, 452 (2007).
- [12] I. H. Deutsch and P. S. Jessen, *Phys. Rev. A* **57**, 1972 (1998).

- [13] R. C. Brown, R. Wyllie, S. B. Koller, E. A. Goldschmidt, M. Foss-Feig, and J. V. Porto, *Science* **348**, 540 (2015).
- [14] S. Trotzky, P. Cheinet, S. Fölling, M. Feld, U. Schnorrberger, A. M. Rey, A. Polkovnikov, E. A. Demler, M. D. Lukin, and I. Bloch, *Science* **319**, 295 (2008).
- [15] S. Trotzky, Y.-A. Chen, U. Schnorrberger, P. Cheinet, and I. Bloch, *Phys. Rev. Lett.* **105**, 265303 (2010).
- [16] H.-N. Dai, B. Yang, A. Reingruber, H. Sun, X.-F. Xu, Y.-A. Chen, Z.-S. Yuan, and J.-W. Pan, [arXiv:1602.05709](https://arxiv.org/abs/1602.05709).
- [17] H.-N. Dai, B. Yang, A. Reingruber, X.-F. Xu, X. Jiang, Y.-A. Chen, Z.-S. Yuan, and J.-W. Pan, *Nat. Phys.* **12**, 783 (2016).
- [18] R. Grimm, M. Weidemüller, and Y. B. Ovchinnikov, *Adv. At. Mol. Opt. Phys.* **42**, 95 (2000).
- [19] P. Windpassinger and K. Sengstock, *Rep. Prog. Phys.* **76**, 086401 (2013).
- [20] V. Finkelstein, P. R. Berman, and J. Guo, *Phys. Rev. A* **45**, 1829 (1992).
- [21] R. Taïeb, P. Marte, R. Dum, and P. Zoller, *Phys. Rev. A* **47**, 4986 (1993).
- [22] O. Mandel, M. Greiner, A. Widera, T. Rom, T. W. Hänsch, and I. Bloch, *Phys. Rev. Lett.* **91**, 010407 (2003).
- [23] B. Paredes and I. Bloch, *Phys. Rev. A* **77**, 023603 (2008).
- [24] F. Gerbier and J. Dalibard, *New J. Phys.* **12**, 033007 (2010).
- [25] M. Aidelsburger, M. Lohse, C. Schweizer, M. Atala, J. T. Barreiro, S. Nascimbene, N. R. Cooper, I. Bloch, and N. Goldman, *Nat. Phys.* **11**, 162 (2015).
- [26] J. Li, W. Huang, B. Shteynas, S. Burchesky, F. Ç. Top, E. Su, J. Lee, A. O. Jamison, and W. Ketterle, *Phys. Rev. Lett.* **117**, 185301 (2016).
- [27] J.-R. Li, J. Lee, W. Huang, S. Burchesky, B. Shteynas, F. Ç. Top, A. O. Jamison, and W. Ketterle, *Nature (London)* **543**, 91 (2017).
- [28] M. Schreiber, S. S. Hodgman, P. Bordia, H. P. Lüschen, M. H. Fischer, R. Vosk, E. Altman, U. Schneider, and I. Bloch, *Science* **349**, 842 (2015).
- [29] J. Schachenmayer, D. M. Weld, H. Miyake, G. A. Siviloglou, W. Ketterle, and A. J. Daley, *Phys. Rev. A* **92**, 041602 (2015).
- [30] A. Kantian, S. Langer, and A. Daley, [arXiv:1609.03579](https://arxiv.org/abs/1609.03579).
- [31] M. Lewenstein, A. Sanpera, and V. Ahufinger, *Ultracold Atoms in Optical Lattices: Simulating Quantum Many-Body Systems* (OUP, Oxford, U.K., 2012).
- [32] C. V. Parker, L.-C. Ha, and C. Chin, *Nat. Phys.* **9**, 769 (2013).
- [33] D. Greif, T. Uehlinger, G. Jotzu, L. Tarruell, and T. Esslinger, *Science* **340**, 1307 (2013).